



# A Non-equipartition Shock Wave Traveling in a Dense Circumstellar Environment around SN 2020oi

Assaf Horesh<sup>1</sup> , Itai Sfaradi<sup>1</sup> , Mattias Ergon<sup>2</sup>, Cristina Barbarino<sup>2</sup> , Jesper Sollerman<sup>2</sup> , Javier Moldon<sup>3,4</sup> , Dougal Dobie<sup>5,6</sup> , Steve Schulze<sup>7</sup> , Miguel Pérez-Torres<sup>3</sup> , David R. A. Williams<sup>4,8</sup> , Christoffer Fremling<sup>9</sup> , Avishay Gal-Yam<sup>7</sup> , Shrinivas R. Kulkarni<sup>10</sup> , Andrew O'Brien<sup>5</sup> , Peter Lundqvist<sup>2</sup> , Tara Murphy<sup>5</sup> , Rob Fender<sup>8</sup>, Shreya Anand<sup>10</sup>, Justin Belicki<sup>9</sup>, Eric C. Bellm<sup>11</sup> , Michael W. Coughlin<sup>12</sup> , Kishalay De<sup>10</sup>, V. Zach Golkhou<sup>11,13</sup> , Matthew J. Graham<sup>14</sup> , Dave A. Green<sup>15</sup> , Matt Hankins<sup>10</sup>, Mansi Kasliwal<sup>10</sup>, Thomas Kupfer<sup>16</sup> , Russ R. Laher<sup>17</sup> , Frank J. Masci<sup>17</sup> , A. A. Miller<sup>18,19</sup> , James D. Neill<sup>9</sup> , Eran O. Ofek<sup>7</sup> , Yvette Perrott<sup>20</sup> , Michael Porter<sup>9</sup>, Daniel J. Reiley<sup>9</sup>, Mickael Rigault<sup>21</sup> , Hector Rodriguez<sup>9</sup>, Ben Rusholme<sup>17</sup> , David L. Shupe<sup>17</sup> , and David Titterington<sup>15</sup>

<sup>1</sup> Racah Institute of Physics, The Hebrew University of Jerusalem, Jerusalem 91904, Israel

<sup>2</sup> Department of Astronomy, The Oskar Klein Center, Stockholm University, AlbaNova, SE-10691 Stockholm, Sweden

<sup>3</sup> Instituto de Astrofísica de Andalucía (IAA, CSIC), Glorieta de las Astronomía, s/n, E-18008 Granada, Spain

<sup>4</sup> Jodrell Bank Centre for Astrophysics, School of Physics and Astronomy, University of Manchester, Manchester M13 9PL, UK

<sup>5</sup> Sydney Institute for Astronomy, School of Physics, University of Sydney, NSW 2006, Australia

<sup>6</sup> ATNF, CSIRO Astronomy and Space Science, P.O. Box 76, Epping, NSW 1710, Australia

<sup>7</sup> Department of Particle Physics and Astrophysics, Weizmann Institute of Science, Israel

<sup>8</sup> Astrophysics, Department of Physics, University of Oxford, Keble Road, Oxford OX1 3RH, UK

<sup>9</sup> Caltech Optical Observatories, California Institute of Technology, Pasadena, CA 91125, USA

<sup>10</sup> Cahill Center for Astrophysics, California Institute of Technology, 1200 E. California Blvd. Pasadena, CA 91125, USA

<sup>11</sup> DIRAC Institute, Department of Astronomy, University of Washington, 3910 15th Avenue NE, Seattle, WA 98195, USA

<sup>12</sup> School of Physics and Astronomy, University of Minnesota, Minneapolis, MN 55455, USA

<sup>13</sup> The eScience Institute, University of Washington, Seattle, WA 98195, USA

<sup>14</sup> Division of Physics, Mathematics, and Astronomy, California Institute of Technology, Pasadena, CA 91125, USA

<sup>15</sup> Astrophysics Group, Cavendish Laboratory, 19 J.J. Thomson Ave., Cambridge CB3 0HE, UK

<sup>16</sup> Kavli Institute for Theoretical Physics, University of California, Santa Barbara, CA 93106, USA

<sup>17</sup> IPAC, California Institute of Technology, 1200 E. California Blvd, Pasadena, CA 91125, USA

<sup>18</sup> Center for Interdisciplinary Exploration and Research in Astrophysics (CIERA) and Department of Physics and Astronomy, Northwestern University, 1800 Sherman Road, Evanston, IL 60201, USA

<sup>19</sup> The Adler Planetarium, Chicago, IL 60605, USA

<sup>20</sup> School of Chemical and Physical Sciences, Victoria University of Wellington, P.O. Box 600, Wellington 6140, New Zealand

<sup>21</sup> Université Clermont Auvergne, CNRS/IN2P3, Laboratoire de Physique de Clermont, F-63000, Clermont-Ferrand, France

Received 2020 June 24; revised 2020 September 6; accepted 2020 September 15; published 2020 November 11

## Abstract

We report the discovery and panchromatic follow-up observations of the young Type Ic supernova (SN Ic) SN 2020oi in M100, a grand-design spiral galaxy at a mere distance of 14 Mpc. We followed up with observations at radio, X-ray, and optical wavelengths from only a few days to several months after explosion. The optical behavior of the supernova is similar to those of other normal SNe Ic. The event was not detected in the X-ray band but our radio observations revealed a bright mJy source ( $L_\nu \approx 1.2 \times 10^{27} \text{ erg s}^{-1} \text{ Hz}^{-1}$ ). Given the relatively small number of stripped envelope SNe for which radio emission is detectable, we used this opportunity to perform a detailed analysis of the comprehensive radio data set we obtained. The radio-emitting electrons initially experience a phase of inverse Compton cooling, which leads to steepening of the spectral index of the radio emission. Our analysis of the cooling frequency points to a large deviation from equipartition at the level of  $\epsilon_e/\epsilon_B \gtrsim 200$ , similar to a few other cases of stripped envelope SNe. Our modeling of the radio data suggests that the shock wave driven by the SN ejecta into the circumstellar matter (CSM) is moving at  $\sim 3 \times 10^4 \text{ km s}^{-1}$ . Assuming a constant mass loss from the stellar progenitor, we find that the mass-loss rate is  $\dot{M} \approx 1.4 \times 10^{-4} M_\odot \text{ yr}^{-1}$  for an assumed wind velocity of  $1000 \text{ km s}^{-1}$ . The temporal evolution of the radio emission suggests a radial CSM density structure steeper than the standard  $r^{-2}$ .

*Unified Astronomy Thesaurus concepts:* Supernovae (1668); Type Ic supernovae (1730); Core-collapse supernovae (304); Radio transient sources (2008); Radio observatories (1350); Optical observation (1169); X-ray transient sources (1852); Transient sources (1851)

*Supporting material:* machine-readable tables

## 1. Introduction

The various paths leading to a core-collapse supernova (SN), the explosive death of a massive star, are still not fully understood. However, thanks to the increasing number of transient discoveries over the last decade, the study and characterization of thousands of SNe have become possible. In particular, the discovery of young SNe, a day to a few days

after explosion, and panchromatic follow-up allow us to probe the properties of the stellar progenitors.

In the optical, early observations led to the discovery of high-excitation narrow emission lines (also known as flash spectroscopy features; e.g., Niemela et al. 1985; Gal-Yam et al. 2014; Groh 2014; Yaron et al. 2017). These features likely originate from a dense confined shell of circumstellar material

(CSM), ejected by the progenitor star only a few years prior to explosion. Early observations of such shells can reveal the composition of the outer envelope of the exploding star before it is mixed with elements produced in the explosion itself.

Radio observations probe the interaction of the SN ejecta with the CSM. The CSM closest to the star has been deposited by mass-loss processes (e.g., stellar winds or eruptive mass ejections). Thus early radio observations of young SNe provide information on the mass-loss history of the progenitor star in its latest evolutionary stage, leading to the explosion. As the mass-loss process is linked to the star just prior to explosion, understanding it empirically is a key element in the overall quest for our understanding stellar death.

Early radio observations have already provided some surprises. For example, PTF 12gzk (Ben-Ami et al. 2012) exhibited early faint radio emission that peaked below 10 GHz several days after explosion and quickly faded beyond detection when the SN was  $\sim 10$  days old (Horesh et al. 2013a). This behavior was also observed in SN 2007gr (Soderberg et al. 2010b) and SN 2002ap (Berger et al. 2002). It may point to a fast (0.2–0.3c) shock wave traveling in a low-density CSM environment. Clearly it can only be captured if observations are undertaken early enough. Such SNe, with relatively high shock-wave velocities, may represent an understudied population of SNe that link normal SNe Ic to relativistic ones. Early radio observations may also play a role in studying new types of transients. For instance, early observations of SN 2018cow (Ho et al. 2019), an optical fast blue transient, revealed a bright plateau of millimeter-wave emission. The early behavior of the millimeter-wave emission is still not well understood, especially when compared to the radio emission at centimeter wavelength, which may be explained by a decelerating circumstellar shock wave (Margutti et al. 2019; A. Horesh et al. 2020, in preparation).

While the study of the recent mass-loss history from massive stars, via radio (and sometimes also X-ray) observations, is important for all types of SNe, that of stripped envelope SNe (of spectral Types IIb/Ib/Ic) is of particular interest. These SNe must have undergone enhanced mass loss in order to lose most of their hydrogen, and in some cases also helium, envelopes. Radio emission has been detected from a number of nearby stripped envelope SNe (e.g., SN 2004cc, SN 2007bg, SN 1990B, SN 1994I, and SN 2003L Chevalier & Fransson 2006; Wellons et al. 2012; Salas et al. 2013 and references therein). A comprehensive view of the ongoing processes in the SN-CSM shock wave can be obtained if X-ray and optical data are combined with radio measurements. Early combined radio to X-ray observations of SN 2011dh (Soderberg et al. 2012; Horesh et al. 2013b) pointed toward a large deviation from equipartition between the shock-wave-accelerated electron energy and the shock-wave-enhanced magnetic field energy. Other examples include SN 2012aw (Yadav et al. 2014), in which the steep radio spectrum observed early on showed a significant inverse Compton cooling at frequencies above 1 GHz, and SN 2013df (Kamble et al. 2016), which also showed signs of electron cooling by inverse Compton scattering in the radio band. The inverse Compton scattering process in these SNe resulted in enhanced X-ray emission. In both SNe, large deviations from equipartition were found (by a factor of  $\sim 200$ ).

The past observations show the considerable diagnostic value resulting from radio observations of young SNe. Here, we report the optical discovery of SN 2020oi, a nearby stripped envelope SN of Type Ic (Section 2). We conducted a

comprehensive radio observing campaign of SN 2020oi with various facilities (Section 3) and also obtained X-ray measurements with the The Neil Gehrels Swift Observatory satellite (Section 4). We present our detailed analysis of the radio measurements in Section 5 and conclude in Section 6.

## 2. Optical Observations

### 2.1. Initial Discovery and Observations

Supernova SN 2020oi (a.k.a. ZTF 20aaelulu) in M100 (NGC 4321; at a distance of  $\approx 14$  Mpc; see Section 2.2) was discovered in *r*-band images obtained by the Zwicky Transient Facility (ZTF; Bellm et al. 2019; Graham et al. 2019; Dekany et al. 2020) on 2020 January 7 at coordinates  $\alpha = 12^{\text{h}}22^{\text{m}}54^{\text{s}}.93$ ,  $\delta = +15^{\circ}49'25.1''$  (J2000.0). It was initially reported to the Transient Name Server (TNS<sup>22</sup>) by the Automatic Learning for the Rapid Classification of Events (ALeRCE) transient broker service (Forster et al. 2020), which feeds off the ZTF public data stream (Patterson et al. 2019). These authors noted that SN 2020oi exhibited a fast rising light curve with an initial *r*-band magnitude of  $17.3 \pm 0.04$ . Inspection<sup>23</sup> of the ZTF partnership survey data (Bellm et al. 2019) showed that SN 2020oi was also detected in the *g* band by the Palomar 48 inch (P48) telescope on Julian Date (JD) 2,458,855.9588, a few hours before the first reported *r*-band detection. As noted in Forster et al. (2020), a non-detection limit of 20.5 in the *r* band was obtained at the position of SN 2020oi by the P48 telescope on 2020 January 4, 2.9 days prior to first detection. Spectroscopic observations carried out using the SOAR telescope revealed that SN 2020oi is an SN Ic (Siebert et al. 2020). Thus, SN 2020oi is one of the nearest stripped envelope supernovae found in the past decade.

Upon discovery, we triggered photometric observations with the Las Cumbres Observatory (LCO) telescope network. In addition to photometric observations, we carried out 16 spectroscopic observations of SN 2020oi over the first three months after discovery using multiple telescopes: the P60 telescope (equipped with SEDM; Blagorodnova et al. 2018), the Nordic Optical Telescope (NOT), the Palomar 200 inch telescope (P200) and the Keck Telescope (KECK). The log of these spectral observations is provided in Table 1 (see also TNS reports on additional photometric measurements by ATLAS, Pan-STARRS and Gaia).

### 2.2. Data Reduction and Analysis

In the following, we adopt the time of explosion (or time of first light) as the midpoint between last non-detection (three days prior to detection) and first detection, and use the same time window for the uncertainty on the explosion time. Throughout the paper we thus assume that SN 2020oi exploded on JD  $2458854.50 \pm 1.46$  (UT 2020 January 6).

The host galaxy M100 has many redshift-independent distance measurements cataloged on NED,<sup>24</sup> and in this paper we adopt a distance of 14 Mpc, corresponding to a distance modulus of  $30.72 \pm 0.06$  mag. According to Schlafly & Finkbeiner (2011) the Milky Way extinction in the direction of M100 is  $E(B - V) = 0.023$  mag, which we will adopt here. As

<sup>22</sup> <https://wis-tns.weizmann.ac.il/>

<sup>23</sup> A comprehensive inspection of the various available data was performed using the GROWTH marshal portal (Bellm et al. 2019).

<sup>24</sup> <https://ned.ipac.caltech.edu>

**Table 1**  
Summary of Optical Spectroscopic Observations

Observation Date	Phase (rest-frame days)	Telescope+Instrument
2020 Jan 11	5.4	P60+SEDM
2020 Jan 14	8.1	NOT+ALFOSC
2020 Jan 18	12.3	P200+DBSP
2020 Jan 23	17.4	P60+SEDM
2020 Jan 23	17.4	P60+SEDM
2020 Jan 25	19.4	P60+SEDM
2020 Jan 29	23.3	P60+SEDM
2020 Jan 29	24.0	NOT+ALFOSC
2020 Feb 5	30.1	P60+SEDM
2020 Feb 14	39.1	P60+SEDM
2020 Feb 18	44.0	NOT+ALFOSC
2020 Feb 21	46.2	P60+SEDM
2020 Mar 3	56.9	P60+SEDM
2020 Mar 12	66.7	NOT+ALFOSC
2020 Mar 22	76.5	KECK+LRIS
2020 Apr 20	106.1	NOT+ALFOSC

described at the end of the section, we estimate the host extinction as 0.13 mag, giving a total  $E(B - V)$  of 0.153 mag.

In Figure 1 we show the absolute Sloan Digital Sky Survey (SDSS)  $g$ -,  $r$ -, and  $i$ -band light curves as well as spline fits to the P48 data. The P48 photometry was reduced with the ZTF production pipeline (Masci et al. 2019), using image subtraction based on the algorithm of Zackay et al. (2016). The LCO photometry was reduced with the pipeline described in Fremling et al. (2016), using image subtraction with template images from the SDSS (Ahn et al. 2014). In Figure 1 we also show the  $gri$  pseudo-bolometric light curve, calculated from the spline fits to the P48 broadband light curves using the method by Ergon et al. (2014), as well as the bolometric light curve using the bolometric corrections by Lyman et al. (2014).

From the spline fits to the P48 broadband light curves we measure rise times to peak  $t_g = 10.2$  days,  $t_r = 11.9$  days, and  $t_i = 12.5$  days, peak absolute magnitudes  $M_g = -17.3$  mag,  $M_r = -17.3$  mag, and  $M_i = -17.0$  mag, and decline rates from the peak  $\Delta M_{g,15} = 2.09$  mag,  $\Delta M_{r,15} = 1.53$  mag, and  $\Delta M_{i,15} = 1.24$  mag.

From the  $gri$  pseudo-bolometric and bolometric light curves we measure rise times to peak  $t_{gri} = 10.8$  days and  $t_{bol} = 10.5$  days, peak bolometric magnitudes  $M_{gri} = -16.5$  mag and  $M_{bol} = -17.2$  mag, and decline rates from the peak  $\Delta M_{gri,15} = 1.64$  mag and  $\Delta M_{bol,15} = 1.54$  mag. The  $r$ -band peak magnitude is within  $1\sigma$  rms from the average value in the distribution of 44 normal SNe Ic from iPTF (C. Barbarino et al. 2020, in preparation). However, SN 2020oi evolves faster than most SNe in this sample, and the  $r$ -band rise time lies at the lower extreme, and the  $r$ -band decline rate at the higher extreme of the distribution.

The SEDM Integrated Field Unit (IFU) spectra were reduced using pySEDM (Rigault et al. 2019), whereas the NOT and P200 spectra were reduced with custom-built long-slit pipelines (Bellm & Sesar 2016). We note that whereas SEDM was primarily constructed to allow classification (see, e.g., Fremling et al. 2020), for this bright nearby supernova the spectral sequence was actually of good quality and also enabled measurements of line velocities.

The sequence of spectra is plotted in Figure 2. The phases in rest-frame days, with respect to the explosion time, are reported next to each spectrum. At 5 days we measure an absorption

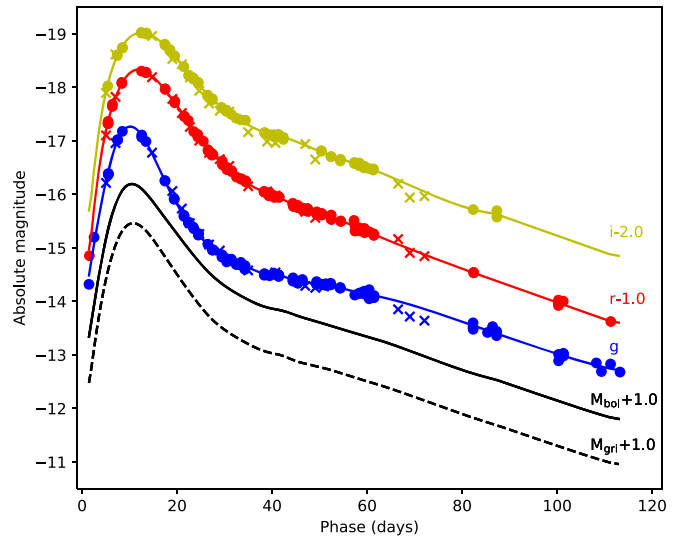


**Figure 1.** Absolute SDSS  $g$ -band (blue),  $r$ -band (red), and  $i$ -band (yellow) light curves as well as bolometric (black solid line) and  $gri$  pseudo-bolometric (black dashed line) light curves. P48 data are shown as filled circles, LCO data as crosses, and spline fits to the P48 data as solid lines.

minimum velocity and an equivalent width of the O I 7774 Å line of  $14,557 \text{ km s}^{-1}$  and  $66 \text{ \AA}$ , respectively; at 12 days ( $r$ -band peak) we measure these to be  $12,443 \text{ km s}^{-1}$  and  $59 \text{ \AA}$ , respectively. Those values are within  $1\sigma$  rms from the average values in the distribution of 56 normal SNe Ic from PTF and iPTF (Fremling et al. 2018), although the velocities are on the higher side of the distribution. All observations will be made public via WISEREP,<sup>25</sup> upon publication.

There appears to be some evidence that the SN exploded in a dense region. We estimate the reddening in two ways. First, we measure the equivalent width of the Na I D line in the high-quality spectrum from Keck, and obtain  $0.74 \pm 0.13 \text{ \AA}$  where the error is estimated by using multiple choices of the continuum level. Alternatively, we can attempt to individually measure 0.55 and  $0.30 \text{ \AA}$  for Na I D2 and D1 independently (by deblending two Gaussians). Using the formalism from Poznanski et al. (2012), this provides estimates of  $E(B - V) = 0.10^{+0.05}_{-0.03}$  mag and  $0.14 \pm 0.05$  mag, respectively.

In addition, we compared the optical colors of SN 2020oi with those of other stripped envelope SNe; following the method of Stritzinger et al. (2018), this results in  $E(B - V) = 0.13$  mag. Although none of the methods used are precise, they are in rough agreement, and in this section we have adopted  $E(B - V) = 0.13$  mag for the host extinction.

### 3. Radio Observations

Radio observations of SN 2020oi were rapidly initiated using several facilities, including the Karl G. Jansky Very Large Array (VLA), the Arcminute Microkelvin Imager—Large Array (AMI-LA; Zwart et al. 2008; Hickish et al. 2018), The Australian Telescope Compact Array (ATCA; Wilson et al. 2011), and the e-MERLIN Telescope. A possible radio detection in the C band was reported on 2020 January 10 (Horesh & Sfaradi 2020a) using the VLA under a public observation undertaken by the National Radio Astronomy Observatory (NRAO). A confirmation of the radio detection was made by the AMI-LA telescope (Sfaradi et al. 2020).

<sup>25</sup> <https://wiserep.weizmann.ac.il>

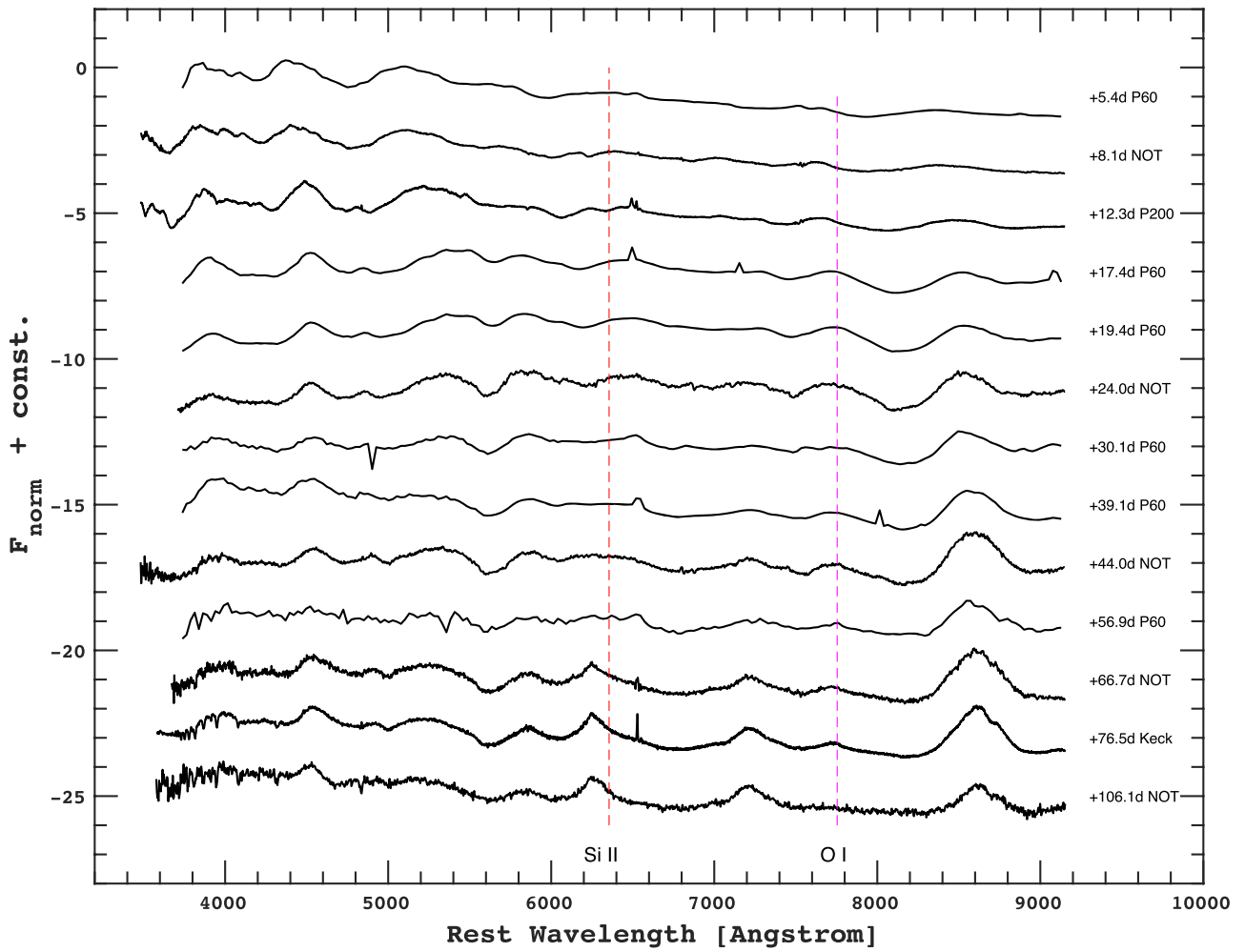


**Figure 2.** The optical spectral evolution of SN 2020oi. The phases, in rest-frame days, are provided next to each spectrum.

Additional detection using the VLA under a public observation undertaken by the NRAO was made on 2020 January 11, in the Q band (Horesh & Sfaradi 2020b). We then initiated a radio observing campaign of SN 2020oi under several director discretionary time (DDT) programs on the following facilities: VLA (PI Horesh); AMI-LA (PI Fender & Horesh); ATCA (PI Dobie); e-MERLIN (PI Perez-Torres & Horesh). Below we report the radio observations by each facility and the data reduction process, and present the results.

### 3.1. The Karl G. Jansky Very Large Array

We observed the field of SN 2020oi with the VLA on several epochs starting 2020 January 10. The observations (both under a public NRAO program and under our DDT program VLA/19B-350; PI Horesh) were performed in the C (5 GHz), X (10 GHz), Ku (15 GHz), K (22 GHz), Ka (33 GHz), and Q (44 GHz) bands. The VLA was in its most compact (D) configuration during the observations conducted up until 2020 January 28, and in the more extended C configuration from 2020 February 10 onward.

We calibrated the data using the automated VLA calibration pipeline available in the Common Astronomy Software Applications (CASA) package (McMullin et al. 2007). Additional flagging was conducted manually when needed. Our primary flux density calibrator was 3C 286, while J1215 +1654 was used as a phase calibrator. Images of the SN 2020oi

field were produced using the CASA task CLEAN in an interactive mode. Each image was produced using 2 GHz bandwidth within the VLA bands, resulting in two images for the C and X bands, three images for the Ku band, and four images for the K, Ka, and Q bands. We also produced images of the full band data for each epoch.

Most observations showed a source at the phase center, which we fitted with the CASA task IMFIT. The image rms was calculated using the CASA task IMSTAT. A summary of the flux density at different observing times and frequencies, for the full band images, is reported in Table 2. We estimate the error of the peak flux density to be a quadratic sum of the image rms, the error produced by CASA task IMFIT, and 10% calibration error. See the online table for more information (see Appendix B for a short version).

### 3.2. The Arcminute Microkelvin Imager—Large Array

Radio observations of the field of SN 2020oi were conducted using the AMI-LA telescope. AMI-LA is a radio interferometer comprising eight antennas of 12.8 m diameter, producing 28 baselines that extend from 18 m up to 110 m in length; it operates with a 5 GHz bandwidth around a central frequency of 15.5 GHz. The first AMI-LA observation of SN 2020oi occurred on 2020 January 11, about five days after explosion, for four hours. We then continued monitoring SN 2020oi with high-cadence observations.

**Table 2**  
Radio Observations of SN 2020oi

$\Delta t$ (days)	Frequency (GHz)	$F_\nu$ (mJy beam $^{-1}$ )	Image rms (mJy)	Telescope
4.72	15.5	10.42 ± 0.62	0.07	AMI-LA
5.15	44	5.12 ± 0.52	0.03	VLA:D
5.3	5.5 <sup>a</sup>	0.52 ± 0.07	0.03	ATCA
5.3	9 <sup>a</sup>	0.46 ± 0.05	0.02	ATCA
5.3	16.7	2.03 ± 0.21	0.03	ATCA
5.3	21.2	2.64 ± 0.27	0.05	ATCA
6.03	44	4.85 ± 0.49	0.03	VLA:D
6.03	33	5.07 ± 0.51	0.01	VLA:D
6.03	22	4.22 ± 0.43	0.01	VLA:D
6.03	15 <sup>a</sup>	3.04 ± 0.34	0.01	VLA:D
6.62	15.5	12.53 ± 0.68	0.05	AMI-LA
7.03	44	3.75 ± 0.38	0.04	VLA:D
7.03	33	4.37 ± 0.44	0.01	VLA:D
7.03	22	4.41 ± 0.46	0.01	VLA:D
7.03	15 <sup>a</sup>	3.80 ± 0.39	0.01	VLA:D
7.03	5.1	0.22 ± 0.06	0.04	e-MERLIN
9.62	15.5	12.8 ± 0.67	0.06	AMI-LA
11.02	33	1.84 ± 0.19	0.02	VLA:D
11.02	22	2.91 ± 0.3	0.01	VLA:D
11.02	15 <sup>a</sup>	4.28 ± 0.44	0.09	VLA:D
11.02	5.1	0.67 ± 0.09	0.04	e-MERLIN
11.76	15.5	11.85 ± 0.66	0.05	AMI-LA
12.72	15.5	11.56 ± 0.64	0.04	AMI-LA
12.99	44	0.95 ± 0.11	0.03	VLA:D
12.99	33	1.36 ± 0.15	0.01	VLA:D
12.99	22	2.21 ± 0.23	0.01	VLA:D
12.99	15 <sup>a</sup>	3.40 ± 0.41	0.09	VLA:D
12.99	5.1	1.16 ± 0.17	0.09	e-MERLIN
13.6	15.5	10.97 ± 0.56	0.05	AMI-LA
14.6	15.5	10.57 ± 0.56	0.07	AMI-LA
16.7	15.5	11.37 ± 0.59	0.08	AMI-LA
17.63	15.5	10.52 ± 0.53	0.08	AMI-LA
17.98	44	0.48 ± 0.06	0.03	VLA:D
17.98	33	0.70 ± 0.08	0.01	VLA:D
17.98	22	1.16 ± 0.14	0.01	VLA:D
17.98	15 <sup>a</sup>	2.34 ± 0.25	0.01	VLA:D
18.62	15.5	9.89 ± 0.51	0.05	AMI-LA
19.59	15.5	9.37 ± 0.5	0.06	AMI-LA
20.69	15.5	9.40 ± 0.49	0.06	AMI-LA
21.56	15.5	9.49 ± 0.49	0.09	AMI-LA
21.98	44	0.35 ± 0.05	0.03	VLA:D
21.98	33	0.54 ± 0.07	0.02	VLA:D
21.98	22	0.97 ± 0.10	0.01	VLA:D
21.98	15 <sup>a</sup>	1.80 ± 0.19	0.01	VLA:D
23.61	15.5	9.61 ± 0.49	0.05	AMI-LA
24.59	15.5	9.12 ± 0.49	0.06	AMI-LA
24.71	5.1	2.18 ± 0.22	0.03	e-MERLIN
27.57	15.5	8.89 ± 0.46	0.05	AMI-LA
29.56	15.5	8.62 ± 0.47	0.07	AMI-LA
30.36	5.1	2.30 ± 0.23	0.02	e-MERLIN
34.93	44	0.20 ± 0.05	0.04	VLA:C
34.93	33	0.29 ± 0.04	0.02	VLA:C
34.93	22	0.48 ± 0.06	0.02	VLA:C
34.93	15	0.77 ± 0.08	0.01	VLA:C
38.36	5.1	2.19 ± 0.25	0.09	e-MERLIN
38.55	15.5	9.70 ± 0.52	0.06	AMI-LA
40.95	33	0.29 ± 0.04	0.02	VLA:C
40.95	22	0.46 ± 0.05	0.01	VLA:C
40.95	15	0.67 ± 0.08	0.01	VLA:C
40.95	10 <sup>a</sup>	1.12 ± 0.13	0.01	VLA:C
40.95	6 <sup>a</sup>	2.78 ± 0.30	0.03	VLA:C
41.93	33	0.32 ± 0.04	0.02	VLA:C
41.93	22	0.47 ± 0.05	0.01	VLA:C
41.93	15	0.71 ± 0.07	0.01	VLA:C

**Table 2**  
(Continued)

$\Delta t$ (days)	Frequency (GHz)	$F_\nu$ (mJy beam $^{-1}$ )	Image rms (mJy)	Telescope
41.93	10 <sup>a</sup>	1.07 ± 0.13	0.01	VLA:C
41.93	6 <sup>a</sup>	2.62 ± 0.28	0.02	VLA:C
45.52	15.5	9.77 ± 0.52	0.09	AMI-LA
52.62	15.5	9.17 ± 0.49	0.06	AMI-LA
57.5	15.5	9.05 ± 0.48	0.05	AMI-LA
59.29	5.1	1.39 ± 0.18	0.07	e-MERLIN
60.29	5.1	1.44 ± 0.16	0.05	e-MERLIN
62.48	15.5	9.15 ± 0.51	0.08	AMI-LA
68.5	15.5	8.57 ± 0.51	0.05	AMI-LA
70.79	33	0.20 ± 0.03	0.01	VLA:C
70.79	22	0.25 ± 0.03	0.01	VLA:C
70.79	15	0.37 ± 0.05	0.01	VLA:C
70.79	10 <sup>a</sup>	0.59 ± 0.09	0.01	VLA:C
70.79	6 <sup>a</sup>	1.55 ± 0.17	0.02	VLA:C
72.55	15.5	10.01 ± 0.56	0.11	AMI-LA
93.76	33	0.09 ± 0.02	0.01	VLA:C
93.76	22	0.20 ± 0.03	0.01	VLA:C
93.76	15	0.27 ± 0.04	0.01	VLA:C
93.76	10 <sup>a</sup>	0.47 ± 0.07	0.01	VLA:C
93.76	6 <sup>a</sup>	1.44 ± 0.15	0.02	VLA:C

**Notes.** A summary of the radio observations conducted with the VLA, AMI-LA, e-MERLIN, and ATCA. The first possible detection reported in Section 3 is not reported here due to high contamination from nearby sources (see Section 3.5). The columns from left to right are as follows: time since explosion in days; observed central frequency in GHz; peak flux density in mJy beam $^{-1}$ ; image rms in mJy; the telescope with which the observation was made. For the VLA observations, the letter after the colon is for the array configuration of the VLA at the time of observation.

<sup>a</sup> These frequencies are suspected to be contaminated from nearby sources and are not used in our analysis (see Section 3.5).

Initial data reduction, flagging, and calibration of the phase and flux were carried out using `reduce_dc`, a customized AMI-LA data reduction software package (e.g., Perrott et al. 2013). Phase calibration was conducted using short interleaved observations of J1215+1654, while daily observations of 3C 286 were used for absolute flux calibration. Additional flagging was performed using CASA. Images of the field of SN 2020oi were produced using CASA task CLEAN in an interactive mode. We fitted the source in the phase center of the images with the CASA task IMFIT, and calculated the image rms with the CASA task IMSTAT. We estimate the error of the peak flux density to be a quadratic sum of the image rms, the error produced by CASA task IMFIT, and 5% calibration error. The flux density at each time and frequency is reported in Table 2.

### 3.3. The e-MERLIN Telescope

We monitored SN 2020oi with e-MERLIN<sup>26</sup> in the C band. Observations were conducted within projects DD9007 and CY10006 and consisted of eight runs between 2020 January 13 and March 6, each observation lasting between 5 and 15 hr. The central frequency was 5.1 GHz with a bandwidth of 512 MHz divided into 512 frequency channels. 3C 286 and OQ 208 were used as amplitude and bandpass calibrators, respectively. The phase calibrator, J1215+1654, was correlated at position

<sup>26</sup> <http://www.e-merlin.ac.uk/>

$\alpha_{\text{J}2000.0} = 12^{\text{h}}15^{\text{m}}03\overset{\text{s}}{.}9791$  and  $\delta_{\text{J}2000.0} = 16^{\circ}54'37\overset{\text{s}}{.}957$  at a separation of  $2.1'$  from the target, and was detected with a flux density of  $0.31 \text{ Jy}$ .

Data reduction was conducted using the e-MERLIN CASA pipeline<sup>27</sup> using version v1.1.16 running on CASA version 5.6.2. Before averaging the data, we applied a phase shift toward the location of an in-beam source located  $1^{\circ}8$  from the target that was used as a reference source to verify the stability of amplitude calibration between epochs. A common model for the phase reference calibrator was used to calibrate and image each run. When possible, a phase self-calibration was conducted on the target with one solution per scan combining all the spectral windows. We produced clean images for the target and the in-beam reference source using `wsclean` (Offringa et al. 2014) with Briggs weighting using a robust parameter of 0.5 and a cell size of 8 mas. The synthesized beam was almost circular with a width of approximately 40 mas. The average flux density of the in-beam reference source is  $0.36 \pm 0.02 \text{ mJy}$ . Results of the measurements are shown in Table 2. We include a 10% uncertainty on the absolute flux density.

### 3.4. The Australian Telescope Compact Array

We conducted two observations of SN 2020oi using the 6A configuration of ATCA under a Target-of-Opportunity proposal (CX456, PI: Dobie) on 2020 January 11 and 18. Observations were carried out in the 4 cm and 15 mm bands, with  $2 \times 2 \text{ GHz}$  bands centered on  $5.5/9 \text{ GHz}$  and  $16.7/21.2 \text{ GHz}$  respectively. We used observations of PKS B1934–638 to determine the flux scale of all observations and the bandpass response of the 4 cm observations. The 15 mm bandpass response was calculated using observations of 1253–055. Observations of 1222+216 were used to calibrate the complex gains of all observations.

The visibility data were reduced using standard MIRIAD (Sault et al. 1995) routines. In addition, we performed one round of phase-only self-calibration (using a small number of iterations) on the 15 mm data. The data were imaged using the MIRIAD clean task with a threshold of  $\sim 8$  times the estimated noise background.

We fit a point source at the phase center using the MIRIAD `imfit` task, allowing all parameters to freely vary. A summary of the flux density at the different observing frequencies is reported in Table 2.

### 3.5. Background Radio Emission

Archival radio data of the field of SN 2020oi are available from the Faint Images of the Radio Sky at Twenty-Centimeters (FIRST) (Becker et al. 1994) and the NRAO VLA Sky Survey (NVSS) (Condon et al. 1998) archives. They show several nearby radio sources at 1.4 GHz, with the closest ones at  $4''$  and  $8''$  from the reported position of the SN. These radio sources may present a concern for observations conducted with relatively large synthesized beams, because the emission from them can contaminate the SN position.

As described previously, during our observations the VLA changed its configuration from the compact D configuration to the more extended C configuration. Our VLA observations in the D configuration had a limited resolution in the Ku band

(lower frequencies were not observed). Hence, we could not resolve the SN emission from the known nearby radio sources. This contamination is visible in the upper left panel of Figure 3, which shows underlying excess emission in the Ku-band image when the VLA was in the D configuration. However, in the upper right panel of this figure, the image of the Ku band when the VLA was in the C configuration shows only negligible contamination. Due to this, flux measurements of Ku-band data taken in the D configuration are reported in Table 2 but are not used in our analysis.

Observations conducted in the C band and at the lower subband of the X band (9 GHz), when the VLA was in the C configuration, are also affected by contamination from the nearby known sources. The lower right image in Figure 3 shows the C-band image of SN 2020oi when the VLA is in the C configuration. This image, which exhibits similar features to the ones shown in the Ku band in the D configuration, shows the excessive emission that affects this band. For convenience, we do not show the 9 GHz image, but it also shows additional emission at the SN position due to the nearby sources. Due to this, flux measurements below 10 GHz that were taken in the C configuration are reported in Table 2 but are not used in our analysis.

AMI-LA has a limited resolution at its observing frequency of 15.5 GHz due to its short baselines. This results in a large synthetic beam of  $\approx 30''$ . Hence, we cannot resolve the SN emission from the emission of the known nearby sources and the diffuse emission from the host at any time. As seen in Figure 3 we only detect a point source, which comprises the SN emission and the nearby sources.

Due to the high declination of the source the synthesized beam of ATCA is highly elongated, and in the 4 cm band (5.5 and 9 GHz) we find it is too elongated to reliably distinguish between emission from the SN and the nearby sources. We therefore do not include these measurements in our analysis.

## 4. X-Ray Observations

### 4.1. Observations and Data Reduction

Swift observed SN 2020oi with its onboard X-ray telescope (XRT; Burrows et al. 2005) in the energy range from 0.3 to 10 keV between 2020 January 8 and February 28. Swift also observed the field in 2005–2006 and 2019. We omit the 2019 data because they are affected by SN 2019ehk. We analyzed all data with the online tools of the UK Swift team,<sup>28</sup> which use the methods described in Evans et al. (2007, 2009) and the software package HEAsoft<sup>29</sup> version 6.26.1 (Blackburn 1995).

### 4.2. Results

To build the light curve of SN 2020oi and examine whether any other X-ray source is present at the SN position, we stack the data of each observing segment. We detect emission at the SN position in data from 2005 to 2006 and in the 2020 data sets. The average count rate in 2005–2006 is  $0.013 \pm 0.001 \text{ counts s}^{-1}$  and its rms is  $0.005 \text{ counts s}^{-1}$  (0.3–10 keV). The count rate of the data from 2020 is comparable. Spectra of the two epochs show no differences to within the errors, corroborating that the same

<sup>28</sup> [https://www.swift.ac.uk/user\\_objects/](https://www.swift.ac.uk/user_objects/)

<sup>29</sup> <https://heasarc.gsfc.nasa.gov/docs/software/heasoft/>

<sup>27</sup> <https://github.com/e-merlin/eMERLINCASApipeline>

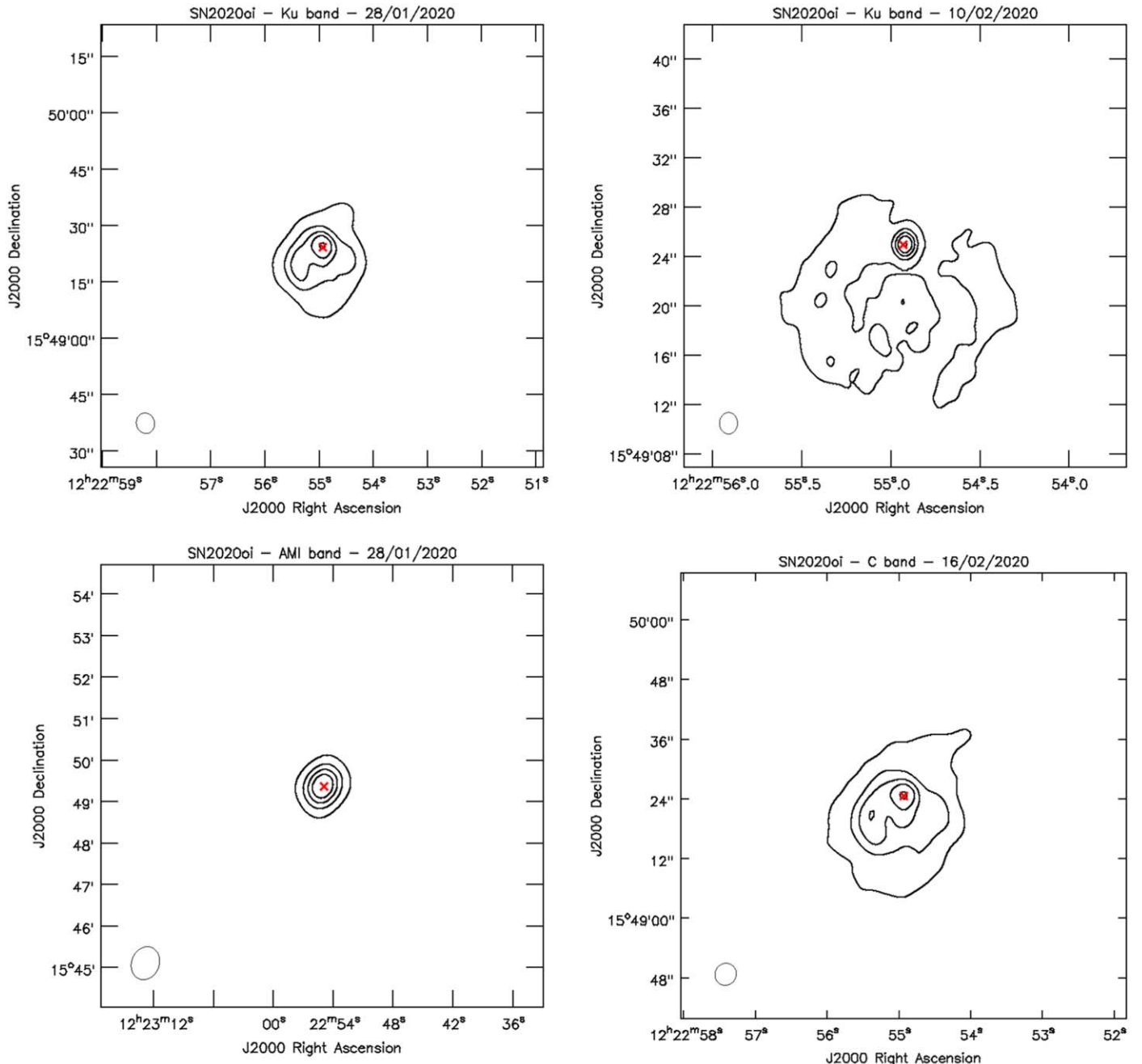


**Figure 3.** Contour maps of the field of SN 2020oi (the SN is marked by a red “ $\times$ ”) for different times and frequencies. These images are examples of how the flux contamination discussed in Section 3.5 varies according to telescope configuration and the observed band. Top panels show images taken with the VLA in the Ku band. The left panel is from 2020 January 28 in the D configuration, while the right panel shows an image from 2020 February 10 in the C configuration. The bottom left panel is an AMI-LA 15.5 GHz image from 2020 January 28. The bottom right image is a VLA C-band image from 2020 February 16. Due to the contamination seen in the Ku-band images taken when the VLA was in the D configuration, and in the VLA C-band images, we do not use these bands (see Section 3.5). The contours represent 10%, 30%, 50%, and 70% of the peak reported in Table 2.

source dominates (the emission), i.e., the SN is not dominating the X-ray emission.

To recover the SN flux, we numerically subtracted the baseline flux. The error of the baseline-subtracted SN data was computed by adding the standard error of the baseline flux in quadrature to the total error. To convert count rate to flux, we extracted a spectrum of the 2005–2006 data set. The spectrum is adequately described with an absorbed power law where the two absorption components represent absorption in the Milky Way and in the host galaxy. The Galactic equivalent neutral hydrogen column

density was fixed to  $2.14 \times 10^{20} \text{ cm}^{-2}$ . The best-fit value of the host absorption is  $1.7_{-0.6}^{+0.7} \text{ cm}^{-2}$  and that of the photon index<sup>30</sup>  $2.9 \pm 0.3$  (all uncertainties at 90% confidence;  $\chi^2 = 209$ , degrees of freedom = 162). To convert the count rate into flux, we use an unabsorbed energy conversion factor of  $4 \times 10^{-11} \text{ erg cm}^{-2} \text{ count}^{-1}$ . Table 3 summarizes the flux measurements. In that table, we report  $3\sigma$  limits for epochs, where the debiased flux level is negative. Furthermore, we applied a 1 day

<sup>30</sup> The photon index is defined by  $A(E) \propto E^{-\Gamma}$ .

**Table 3**  
Swift/XRT Photometry

Time (MJD)	Phase (days)	Flux ( $10^{-13}$ erg cm $^{-2}$ s $^{-1}$ )
58,856.96	2.96	$1.02 \pm 0.98$
58,857.96	3.96	$1.48 \pm 1.56$
58,858.96	4.96	<2.20
58,859.96	5.96	<2.26
58,860.96	6.96	<4.48
58,876.96	22.96	$1.35 \pm 2.85$
58,887.96	33.96	<5.08
58,898.96	44.96	$2.72 \pm 2.32$
58,906.96	52.96	<4.69

binning. As shown in the table, we do not find any significant X-ray emission from SN 2020oi, with an approximate upper limit of  $\lesssim 5 \times 10^{-13}$  erg cm $^{-2}$  s $^{-1}$  ( $L_X \lesssim 1.2 \times 10^{40}$  erg s $^{-1}$ ).

## 5. Radio Data Modeling and Analysis

In this section we analyze and model the radio data shown in Section 3 using the SN-CSM interaction model described in Chevalier (1981). In the Chevalier model the SN ejecta drive a shock wave into the CSM. As a result, electrons are accelerated at the shock front and gyrate in the presence of a magnetic field that is amplified by the shock wave. This gives rise to synchrotron emission, which is usually observed in radio waves (Chevalier 1982). The synchrotron emission from the SN can also be absorbed, e.g., by synchrotron self-absorption (SSA; Chevalier 1998) and/or by free-free absorption (FFA; Weiler et al. 2002). Past observations have shown that in most cases for SNe Ic, SSA is dominant over FFA (e.g., Chevalier & Fransson 2006), and we thus use the SSA model described by Chevalier (1998) here.

In the CSM shock-wave model, the accelerated relativistic electrons have a power-law energy distribution,  $N(E) = N_0 E^{-p}$ . In the SSA-only model, the flux from the SN in the optically thick regime ( $\nu < \nu_a$ , where  $\nu_a$  is the frequency at which the optical depth is around unity) is described by

$$S_\nu \propto \frac{\pi R^2}{D^2} B^{-1/2} \nu^{5/2}. \quad (1)$$

Above  $\nu_a$ , in the optically thin regime, the flux is

$$S_\nu \propto \frac{4\pi f R^3}{3D^2} N_0 B^{(p+1)/2} \nu^{-(p-1)/2}, \quad (2)$$

where  $R$  is the radius of the radio-emitting shell,  $B$  is the magnetic field strength,  $D$  is the distance to the SN, and  $f$  is the emission filling factor.

Measurements of the radius of the radio-emitting shell and of the magnetic field at the shock front can be obtained at any given time using the observed radio spectral peak,  $F_{\nu_a}$ , and peak frequency  $\nu_a$ , at that time (Chevalier & Fransson 2006). Assuming  $p = 3$ , the radius is given by

$$R = 4.0 \times 10^{14} f_{eB}^{-1/19} \left( \frac{f}{0.5} \right)^{-1/19} \left( \frac{F_{\nu_a}}{\text{mJy}} \right)^{9/19} \times \left( \frac{D}{\text{Mpc}} \right)^{18/19} \left( \frac{\nu_a}{\text{5 GHz}} \right)^{-1} \text{cm}, \quad (3)$$

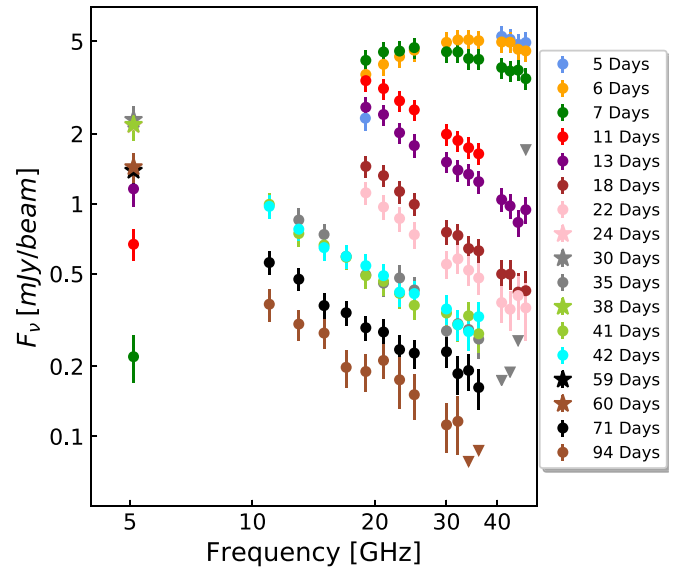


**Figure 4.** Radio emission as a function of observing frequency for different epochs. These radio measurements were produced by the VLA, e-MERLIN, and ATCA as described in Section 3 and reported in Table 2.

and the magnetic field strength is

$$B = 1.1 f_{eB}^{-4/19} \left( \frac{f}{0.5} \right)^{-4/19} \left( \frac{F_{\nu_a}}{\text{mJy}} \right)^{-2/19} \times \left( \frac{D}{\text{Mpc}} \right)^{-4/19} \left( \frac{\nu_a}{\text{5 GHz}} \right) \text{G} \quad (4)$$

where  $f_{eB}$  is the ratio between the fraction of shock-wave energy deposited in relativistic electrons ( $\epsilon_e$ ) and the fraction converted to magnetic fields ( $\epsilon_B$ ).

In our analysis below, we will model the data in several ways (similar to, e.g., Horesh et al. 2013b). First, data from observing epochs where a radio peak is present will be analyzed individually by fitting models of single-epoch spectra to those measurements. These individual fits will provide single measurements of the shock-wave radius, the magnetic field, and the power law of the electron energy distribution. Second, we model the temporal evolution of single frequencies. Then, we also attempt to perform a combined fit of the full data set that includes also the time evolution of the radio emission.

### 5.1. Single-epoch Spectral Modeling

Here we perform individual analysis of the broadband spectral radio data obtained five to thirteen days after explosion, according to Equations (3) and (4). The individual spectrum (see online Table; see Appendix B for a short version) is shown in Figure 4. Note that we do not use the AMI-LA data in our analysis since they suffers from contamination as described in Section 3.5, which leads to large uncertainties in the AMI-LA flux measurements. The VLA Ku-band data are also not included in our analysis here (see Section 3.5).

To obtain the spectral peak and frequency, we fit a generalized form of Equation (4) in Chevalier (1998) to the radio spectrum. The free parameters here are  $F_{\nu_a}(t_a)$  and  $\nu_a$ . The spectral index of the optically thin regime,  $\beta$ , is also a free parameter in the fitted model. Since we fit to a single epoch we use  $t = t_a$ , where  $t$  is the time of observation.

**Table 4**  
SN2020oi—Radio Spectral Fits and the Derived Equipartition Shock-wave Parameters

$t_a$ (days)	$F_{\nu_a}(t_a)$ (mJy beam $^{-1}$ )	$\nu_a$ (GHz)	$\beta$	$\chi^2_r$ (dof)	$R$ ( $10^{15}$ cm)	$B$ (G)	$v_{sh}$ ( $10^4$ km s $^{-1}$ )	$\dot{M}$ ( $10^{-5} M_{\odot}$ yr $^{-1}$ )
5	$5.24 \pm 0.51$	$31.4 \pm 1.8$	$-1.04 \pm 0.31$	0.10 (1)	$1.70 \pm 0.26$	$3.33 \pm 0.61$	$3.9 \pm 1.3$	$1.4 \pm 1.0$
6	$4.51 \pm 0.61$	$23.7 \pm 1.7$	$-0.53 \pm 0.37$	0.06 (8)	$2.10 \pm 0.35$	$2.55 \pm 0.53$	$4.0 \pm 1.2$	$1.2 \pm 0.8$
7	$4.40 \pm 0.84$	$20.4 \pm 1.7$	$-0.77 \pm 0.39$	0.04 (9)	$2.41 \pm 0.44$	$2.21 \pm 0.56$	$4.0 \pm 1.1$	$1.3 \pm 0.8$
11	$4.07 \pm 0.78$	$12.6 \pm 0.6$	$-1.31 \pm 0.15$	0.02 (5)	$3.76 \pm 0.64$	$1.37 \pm 0.33$	$4.0 \pm 0.9$	$1.2 \pm 0.7$
13	$3.84 \pm 0.39$	$9.89 \pm 0.38$	$-1.25 \pm 0.12$	0.19 (9)	$4.66 \pm 0.83$	$1.08 \pm 0.20$	$4.1 \pm 0.9$	$1.0 \pm 0.6$
20.4 ± 1.8	$2.21 \pm 0.37$	5.1	...	0.69 (3)	$6.96 \pm 1.70$	$0.59 \pm 0.16$	$3.9 \pm 1.0$	$0.8 \pm 0.4$

**Note.** The first five rows show a summary of the radio peak fit at five separate epochs and the derived measurements of the shock-wave radius, magnetic field strength, shock-wave velocity, and mass-loss rate assuming a wind velocity of  $v_w = 1000$  km s $^{-1}$  (see details of parameters used in Section 5.1). The last row shows a summary of the radio peak fit for the 5.1 GHz light curve measured by e-MERLIN (see Section 5.2). As we note in the main text, the radius and magnetic field here are calculated assuming  $p = 3$ . An uncertainty of  $\Delta p = \pm 0.5$  will result in additional uncertainty of 17% and 27% in  $R$  (and thus also in  $v_{sh}$ ) and  $B$ , respectively. The uncertainty  $\Delta t_a$  was used to calculate the uncertainty in the shock velocity and the mass-loss rate; for the VLA spectra we use  $\Delta t_a = 1.46$  days as mentioned in Section 2.2. Note that a deviation from equipartition (such as the one we discuss in the main text) will significantly change the estimates of  $R$ ,  $v_{sh}$ , and  $B$ .

(This table is available in machine-readable form.)

The spectral index of the optically thin synchrotron emission is assumed to be a function of the electron energy power-law index. In the non-cooling regime, the spectral index is defined as  $\beta = -(p - 1)/2$ . However, the estimation of the spectral index  $\beta$  and hence  $p$  in our case has some limitations. Since in the first three epochs the data do not span a wide enough frequency range after the peak, we probably do not see the radio emission settle fully into the optically thin regime. Thus, the best-fit spectral indices in these epochs do not represent the real values well enough. In addition, the spectral index of the electron energy density may be affected by electron cooling as discussed in Section 5.4. When cooling is present the spectral index will be steeper than what is expected according to the  $p$ -based relation above. Due to these drawbacks, in our analysis below, we use  $p = 3$  based on the average value observed in past stripped envelope SNe (e.g., Chevalier & Fransson 2006; Soderberg et al. 2012; Horesh et al. 2013b). If  $p = 3$  then the expected spectral index is  $\beta = -1$ , which is the value we eventually observe at late times (Section 5.4). If the real  $p$  is in the range  $2.5 < p < 3.5$ , this will add an additional uncertainty to our analysis below (see Table 4).

The results of the fitting procedure described above are summarized in Table 4 (including the minimum  $\chi^2_r$ , where  $\chi^2_r = \chi^2/\text{dof}$ , and dof = degrees of freedom), and the observed radio emission together with the best-fit models are shown in Figure 5. The radius of the emitting shell and the magnetic field strength are calculated using Equations (3) and (4) assuming equipartition with  $\epsilon_e = \epsilon_B = 0.1$  (see, however, the discussion of the effect of non-equipartition on these estimates in Section 5.5), and also assuming  $p = 3$  (Table 4). The shock-wave velocity, early on, is on average  $\approx 4 \times 10^4$  km s $^{-1}$  (see, however, Section 5.5). This velocity represents the velocity of the leading edge of the SN ejecta and thus is expected to be higher by a factor of a few than the photospheric velocities measured using the optical emission, which originates from deeper and slower regions within the SN ejecta. Therefore, it is not surprising that the velocity we measure here is a factor of  $>2$  higher than the photospheric velocity we measure at early times (Section 2.2).

A simple comparison diagnostic tool of the shock-wave velocity is the so-called Chevalier diagram (e.g., Chevalier 1998). This is a diagram of the measured  $L_{\nu_a} - t_a \nu_a$  plane (where

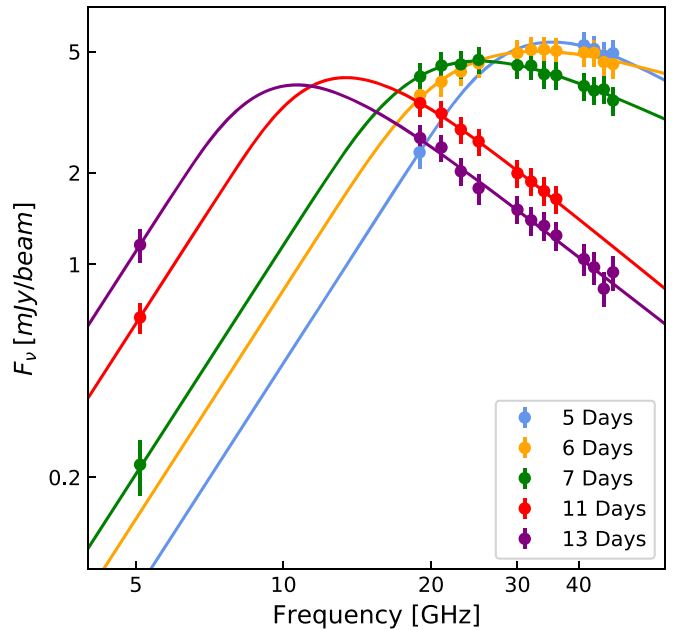


**Figure 5.** Model fitting of Equation (4) in Chevalier (1998) to the observed radio spectra containing information about the spectral peak (using  $\chi^2$  minimization fitting to each epoch separately; see Section 5.1).

$L_{\nu_a}$  is the peak luminosity), which is intersected by diagonal lines of equal velocity. We plot the radio peak measurement of SN 2020oi (six days after explosion) in Figure 6, together with a small sample of measurements of other SNe Ic. As shown in the figure, the SN-CSM shock-wave velocity of SN 2020oi is quite similar to the ones measured in other normal SNe Ic.

We next assume that the CSM originates from stellar winds. We also make the usual assumption that the mass-loss rate and wind velocity were constant on average in the period of time during which the CSM that the SN ejecta interacts with was created. The CSM in this case has a density structure of  $\rho \propto \dot{M}/(v_w r^2)$ , where  $\dot{M}$  is the mass-loss rate and  $v_w$  is the wind velocity. As the energy density of the magnetic energy is a fraction of the shock-wave energy density, which depends

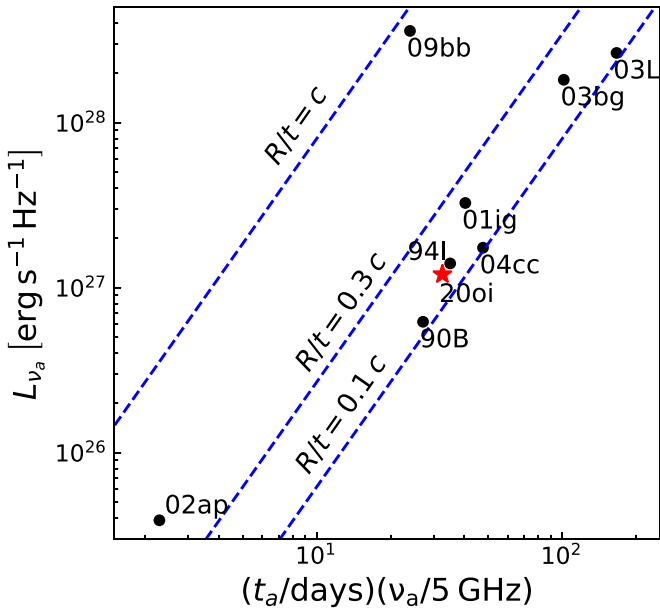


**Figure 6.** Chevalier’s diagram showing the peak luminosity vs. peak frequency and time. Black circles mark other known SNe Ic. For SN 1990B, SN 1994I, SN 2001ig, SN 2002ap, SN 2003L, and SN 2003bg we used the values reported in Chevalier & Fransson (2006). For SN 2009bb we used the value reported by Soderberg et al. (2010a). For SN 2004cc we used the value reported by Wellons et al. (2012). The red star marks SN 2020oi as fitted to the spectrum, six days after explosion (Table 4). Lines of equal  $R/t$  are plotted in blue, according to Equation (3).

on the CSM density, we can derive, using the magnetic field strength and the shock-wave radius found above, the mass-loss rate

$$\dot{M} = 5.2 \times 10^{-6} \left( \frac{\epsilon_B}{0.1} \right)^{-1} \left( \frac{B}{1 \text{ G}} \right)^2 \times \left( \frac{t}{10 \text{ days}} \right)^2 \left( \frac{v_w}{1000 \text{ km s}^{-1}} \right) M_\odot \text{ yr}^{-1}. \quad (5)$$

Estimating the mass-loss rate alone requires an assumption of the wind velocity. Stripped envelope SNe are believed to originate from Wolf–Rayet stars, which have fast winds of the order of  $v_w = 1000 \text{ km s}^{-1}$  (Chevalier & Fransson 2006; Smith 2014). Adopting the above wind velocity, we estimate the mass-loss rate at various epochs (see Table 4). The average mass-loss rate from the progenitor of SN 2020oi is  $\dot{M} = 1.2 \times 10^{-5} M_\odot \text{ yr}^{-1}$  (see, however, Section 5.5), which is typical of normal SNe Ic (e.g., Chevalier & Fransson 2006).

### 5.2. Single-frequency Temporal Analysis

Here we analyze the time evolution for individual observed frequencies. At 5.1 GHz, the e-MERLIN observations cover both the rising and declining phases in the light curve. Thus, we model the transition from optically thick to optically thin emission at this frequency. Due to the early peak time in the higher observed frequencies, the VLA single-frequency light curves does not span a wide enough range for a full fit to the light curve. Therefore, for those frequencies we only fit a power law in time for the decaying light curves observed by the VLA. Finally, we evaluate the excessive emission contaminating the flux measurements obtained by AMI-LA, and use its light curve to estimate the shock parameters (see Appendix A for a detailed discussion).

The temporal evolution of the radio emission in both the optically thick and thin regimes is modeled with power laws. Model 1 of Chevalier (1998) assumes  $R \sim t^m$  and  $B \sim t^{-1}$  and that the temporal evolution of the flux is  $F_\nu \sim t^b$  where  $b = -(p + 5 - 6m)/2$  (optically thin regime) and  $F_\nu \sim t^a$  where  $a = 2m + 0.5$  (optically thick regime). These definitions of  $a$  and  $b$  are valid if electron cooling does not affect the emission in the observed frequency.

We fit a generalized form of Equation (4) in Chevalier (1998) to the 5.1 GHz radio light curve measured by e-MERLIN. The free parameters here are  $F_{\nu_a}(t_a)$ ,  $t_a$ , and the temporal power-law indices  $a$  and  $b$ , defined above. Since we fit a single-frequency light curve, we use  $\nu = \nu_a$ , where  $\nu$  is the observed frequency. The resulting power-law indices are  $a = 2.60 \pm 0.32$  and  $b = -0.81 \pm 0.17$ . The fitted peak flux at 5.1 GHz is  $F_{\nu_a} = 2.21 \pm 0.37 \text{ mJy}$  at  $20.4 \pm 1.8$  days after explosion ( $\chi^2_r = 0.69$ , dof = 3). We used the peak at 5.1 GHz to calculate  $R$ ,  $B$ ,  $v_{\text{sh}}$ , and  $\dot{M}$  (we assume  $p = 3$ ,  $v_{\text{sh}} = R/t_a$ , and  $v_w = 1000 \text{ km s}^{-1}$ ) and we report them in Table 4.

We now examine the time evolution of the radio emission as it is manifested in the VLA K, Ka, and Q bands. We use  $\chi^2$  minimization to fit a power law to the declining regimes of the light curves, starting 11 days after explosion since the flux at earlier epochs is around peak for all observed bands. We divide our analysis into two regimes: first we fit for times  $\leq 22$  days, since our analysis suggests that electron cooling takes place up to this time (see Section 5.4). We then fit a power law for times  $\geq 35$  days because electron cooling is no longer significant. The fitting results in the K band and Ka band using data from 11 to 22 days after explosion are  $b = -1.67 \pm 0.14$  ( $\chi^2_r = 0.97$ , dof = 1) and  $b = -1.83 \pm 0.10$  ( $\chi^2_r = 0.44$ , dof = 1), respectively. When using data from 35 to 94 days after explosion the power law in the K band is  $b = -0.97 \pm 0.10$  ( $\chi^2_r = 0.63$ , dof = 2), while in the Ka band we get  $b = -1.03 \pm 0.26$  ( $\chi^2_r = 3.33$ , dof = 2). The fit of Q-band data from 11 to 22 days gives  $b = -1.37 \pm 0.12$  ( $\chi^2_r = 2.2$ , dof = 2). This band was observed again only 35 days after explosion and was not detected.

We fitted, using the same type of analysis applied to the e-MERLIN data, the light curve of the radio emission obtained by the AMI-LA telescope, after removing the estimated background emission discussed in Section 3.5 (see Appendix A). This resulted in a shock velocity of  $v_{\text{sh}} \approx (4.8 \pm 1.4) \times 10^4 \text{ km s}^{-1}$ . While this velocity is somewhat higher than the velocities we derived earlier on, it is consistent within  $1\sigma$  with the previously measured velocities (see Table 4). Note that the flux from the quiescent sources that contaminate the AMI measurement may experience slight variations, thus increasing the uncertainty of the AMI fitting results. Thus, the analysis of the AMI data should be treated with caution, and so should any estimated property that is based on it.

### 5.3. Broadband Spectrum Temporal Analysis

The full time and spectral evolution of the self-absorbed synchrotron emission can be described by introducing a parameterized model such as the one shown in Equation (4) in Chevalier (1998). Below we perform a multi-frequency multi-epoch  $\chi^2$  minimization fit of this model to the SN 2020oi radio data. The free parameters in this process are the peak flux  $F_{\nu_a}(t_a)$ , its frequency  $\nu_a$ , and the spectral index  $\beta$ . The indices of the power laws of the light curve with time,  $a$  (optically thick) and  $b$  (optically thin), are also free parameters in this fitting process.

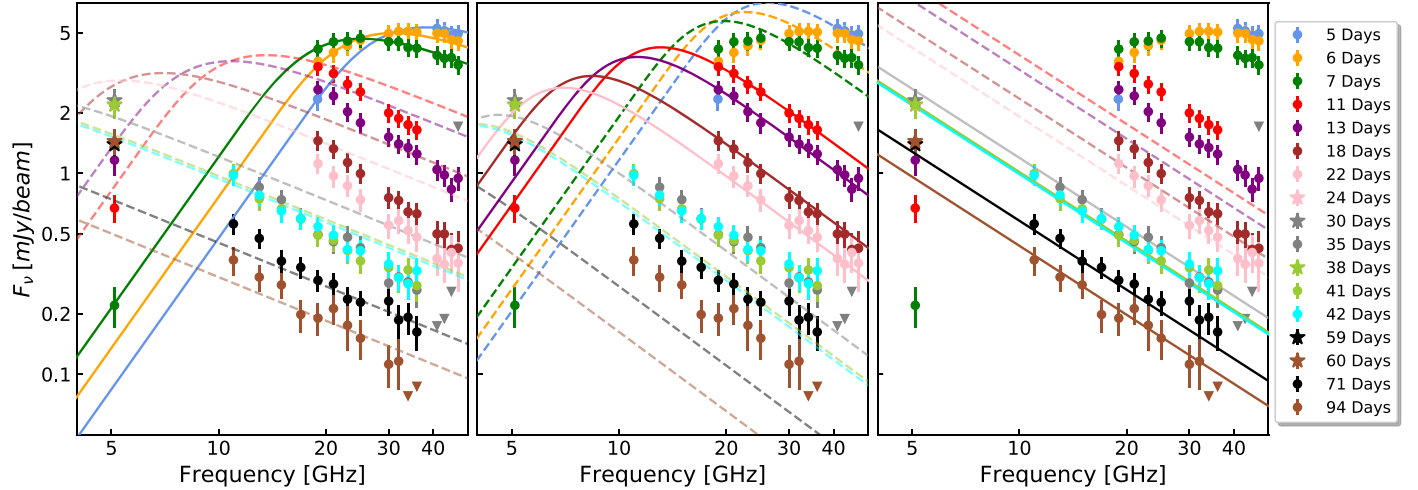


**Figure 7.** The left and the middle panels show model fitting of Equation (4) in Chevalier (1998) to the spectra of SN 2020oi at different epochs. We fit the peak parameters  $F_{\nu_a}(t_a)$  and  $\nu_a$ , the spectral slope  $\beta$ , and the time evolution slopes  $a$  and  $b$ . In the left panel we assume  $t_a = 7$  days while in the middle panel we assume  $t_a = 13$  days. The left panel shows the results of fitting the first three epochs only (solid), and the extrapolated spectra (dashed) at later times. The middle panel shows the results of fitting the data taken 11–24 days after explosion (solid), and the extrapolated spectra (dashed) at different times. The right panel shows the results of fitting a power law in frequency and time to the data starting 30 days after explosion. Since our late-time observations do not constrain the radio peak we cannot make use of the model fitted above. The fitted spectra are shown in the right panel (solid), together with the extrapolated spectra (dashed) at early times.

Since the full optically thick to optically thin spectrum seems to be captured only in the first three observing epochs, we first use only those epochs in a combined fit. Adopting  $t_a = 7$  days, our best-fit parameters are a peak flux of  $4.38 \pm 0.62$  mJy and frequency of  $20.2 \pm 4.0$  GHz. The spectral index is  $\beta = -0.72 \pm 0.40$ , while the indices of the power laws of the optically thick and thin regimes of the light curve are  $a = 3.0 \pm 1.0$  and  $b = -1.4 \pm 0.9$ , respectively. The resulting  $\chi^2_r$  in this case is 0.12 (dof = 24). The power laws of the temporal evolution have large uncertainties and therefore should be treated carefully. We then evolve this fitted model to future time and extrapolate the radio emission to that expected in our additional observing epochs. While our fit describes the first three epochs well, as shown in the left panel of Figure 7, it does a poor job in describing the emission at later times. Also, the spectral index at later times is much steeper than the spectral index early on. However, as noted earlier (Section 5.1), the shallow spectral index in the optically thin regime may be due to having data only in frequencies that are very close to the radio peak frequency. Thus, there is a good chance that we are only witnessing the transition to the optically thin regime.

In Section 5.4 we argue that electron cooling acts in early times. However, it is most significant around the optical peak luminosity, which is after the first three epochs. Additionally, we see some change in the spectral index behavior between the VLA data obtained on days 11–22 and VLA data obtained afterwards. Thus, we next perform a fit to data that we obtained between 11 and 24 days after explosion. Adopting  $t_a = 13$  days here, our best-fit parameters are a peak flux of  $3.75 \pm 0.64$  mJy and frequency of  $10.6 \pm 1.4$  GHz. The spectral index is  $\beta = -1.31 \pm 0.44$ , while the indices of the power laws of the optically thick and thin regimes of the light curve are  $a = 1.6 \pm 1.1$  and  $b = -1.86 \pm 0.63$ , respectively. The resulting  $\chi^2_r$  in this case is 0.26 (dof = 41). We note here, as in the previous fit, that the power laws of the temporal evolution have large uncertainties and therefore should be treated carefully. The middle panel of Figure 7 shows our fitted model, including extrapolations of the radio emission at epochs that are not used in the fitting process. As in the previous fit, the extrapolation of the current model to earlier

and later times does not represent well the measurements at these times (see discussion below).

We next examine the late-time emission by fitting flux measurements at times  $\geq 35$  days after explosion. Since our observations at these times are not constraining the peak we do not fit the same model we fitted above. Instead, we fit an optically thin emission that is described by a power law in frequency and time, i.e.,  $F_\nu(t) \sim \nu^\beta t^b$ , where  $\beta$  and  $b$  are free parameters. Our modeling suggests  $\beta = -1.14 \pm 0.14$  and  $b = -1.02 \pm 0.09$  ( $\chi^2_r = 1.64$ ; dof = 62). The right panel of Figure 7 shows our fitted model, including extrapolations of the radio emission model to epochs not used in the fitting process. We do not show the extrapolated lines of the first three epochs since they exhibit the transition from optically thick to optically thin emission. As the figure shows, while the data can be described quite well by the model at times  $\geq 35$  days after explosion, the model prediction for emission at earlier times deviates significantly from the observed radio emission.

The rapid temporal evolution shown in the middle panel of Figure 7 (between 11 and 24 days) is expected as electron cooling takes place. However, later on, the time evolution approaches  $t^{-1}$  (as shown in the right panel of Figure 7) when the electron cooling no longer affects the emission in the observed frequencies. This is also the reason why the extrapolated radio emission from each fit over- or underpredicts the observed emission in the time preceding or following the time period in which the fit was done. Since in addition to the variations in temporal behavior, there is a large uncertainty in the temporal power-law parameters in each fit, we refrain from using the combined fits of temporal behavior to estimate the shock-wave parameters (e.g., shock-wave radius) because the uncertainty of these estimates will be so large as to render them useless. Moreover, considering the single-epoch modeling results together with the overall temporal behavior of the decreasing peak flux points to a deviation from the standard simplistic model of a shock wave moving at a constant velocity in a spherical CSM structure with a density structure of  $\rho_{\text{CSM}} \propto r^{-2}$ . This might be explained by a shock wave traveling in a more complex CSM density structure.

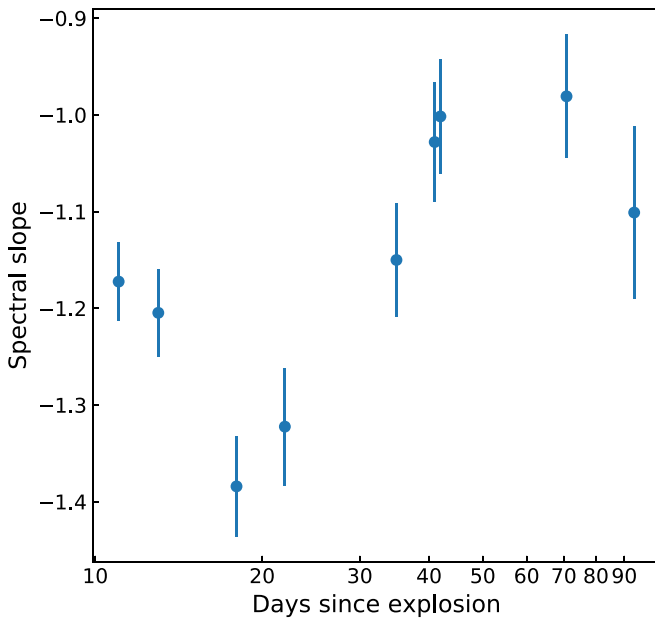


**Figure 8.** Spectral slope measured at different times by fitting a power law to the optically thin regime of the spectrum. Observations of the Ku band when the VLA was in the D configuration, and of the C band and lower-frequency X band when it was in the C configuration, were not used to fit the power law, as described in Section 3.5.

#### 5.4. Electron Cooling

In the CSM interaction model described in Section 5 we assumed a fixed electron energy power law of  $p = 3$ , when translating the radio peak flux and frequency measurements to estimates of  $R$  and  $B$ . We already saw in the previous section that the spectral index deviates from the expected value of  $\beta = -1$  (if  $p = 3$  and  $\beta = -(p - 1)/2$ ). We further test this by measuring the spectral slope  $\beta$  in the optically thin regime at different times, starting from day 11 after explosion. As discussed in Section 3.5, the observations in the Ku band when the VLA was in the D configuration, and in the C band when it was in the C configuration, suffer from flux contamination. Therefore, we removed these observations when fitting the power law to the optically thin regime. The evolution of the spectral slope in time is shown in Figure 8.

As shown in the figure, the spectral index varies with time. Between 11 and 22 days the spectral index is steeper than the expected value of  $\beta = -1$  (a similar behavior was observed in SN 2012aw; Yadav et al. 2014). A possible explanation for this behavior is electron cooling, due to either synchrotron cooling or inverse Compton cooling (see a discussion in Bjornsson & Fransson 2004). In these two former scenarios, if the cooling timescale is shorter than the adiabatic timescale, then the flux above a certain cooling frequency is reduced compared to the non-cooling SSA-only model, effectively leading to a steeper spectral index. Also, it seems that after  $\sim 40$  days, the spectral index settles to a value of  $\beta \approx -1$ .

The synchrotron cooling frequency is

$$\nu_{\text{syn-cool}} = \frac{18\pi m_e c q_e}{\sigma_T^2 B^3 t^2}, \quad (6)$$

where  $m_e$  is the electron mass,  $q_e$  is a unit charge, and  $\sigma_T$  is the Thomson cross section. Using this equation with the values of the magnetic field we found in Section 5.1, we find that the synchrotron cooling frequency is  $\nu_{\text{syn-cool}} > 200$  GHz at all

times and thus does not affect the radio emission at the observed frequencies. It is more probable then that inverse Compton cooling is the dominant process here, which leads to the steep spectral index we observe.

In the inverse Compton case, the cooling frequency is evolving as follows:

$$\nu_{\text{comp}} \approx 0.324 \left( \frac{L_{\text{bol}}}{2 \times 10^{42} \text{ erg s}^{-1}} \right)^{-2} \left( \frac{\epsilon_B}{0.1} \right)^{1/2} \times \left( \frac{\dot{M} [10^{-6} M_{\odot} \text{ yr}^{-1}]}{v_w [10 \text{ km s}^{-1}]} \right)^{1/2} \left( \frac{v_{\text{sh}}}{10^4 \text{ km s}^{-1}} \right)^4 \text{ GHz}. \quad (7)$$

Note that the cooling frequency depends on  $\epsilon_B$ , and in addition the estimates of  $v_{\text{sh}}$  and  $\dot{M}$  using the radio peak data also depend on the ratio between the microphysical parameters ( $\epsilon_e/\epsilon_B$ ). A constraint on the inverse Compton cooling frequency can thus be translated into a constraint on  $\epsilon_B$ , assuming a value for  $\epsilon_e$ . In the case of SN 2020oi, we assume that the Compton cooling frequency rises above our observed range  $\gtrsim 40$  GHz roughly 30–40 days after explosion. Using this in combination with the estimate of observed bolometric luminosity (from our measurements in Section 2) at that time,  $L_{\text{bol}} \sim 2.7 \times 10^{41} \text{ erg s}^{-1}$ , and also assuming  $\epsilon_e \approx 0.1$ , results in the limit  $\epsilon_B \lesssim 0.0005$ . Thus we find that there is deviation from equipartition with  $\epsilon_e/\epsilon_B \gtrsim 200$ . (We note that decreasing the assumed value of  $\epsilon_e$  by an order of magnitude will change our estimate of the latter ratio by a factor of  $\sim 3$  only.) This deviation from equipartition is similar to the one found in both SN 2012aw and SN 2013df.

We next estimate the expected X-ray emission as a result of the inverse Compton process. According to Equation (32) in Chevalier & Fransson (2006), and adopting a maximum bolometric luminosity value<sup>31</sup> of  $L_{\text{bol}} \sim 2.3 \times 10^{42} \text{ erg s}^{-1}$ , the maximum expected inverse Compton X-ray emission is  $\approx 1.2 \times 10^{39} \text{ erg s}^{-1}$ . As one can see, this is below our observed limit of  $L_x < 10^{40} \text{ erg s}^{-1}$  (Section 4). Thus, unfortunately, deriving any additional constraints, using the X-ray observations, is not possible here.

#### 5.5. The Effect on Non-equipartition on Estimates of Shock-wave Parameters

The estimates of shock-wave parameters  $R_p$  and  $B_p$  and the derived estimates of  $v_{\text{sh}}$  and  $\dot{M}/v_w$  in Section 5.1 are based on the assumption of equipartition. The derived values of these parameters will change once the deviation from equipartition that we find is included. Adopting  $\epsilon_e/\epsilon_b \gtrsim 200$  will result in a reduction in the shock-wave radius by  $\gtrsim 24\%$  (and the shock-wave velocity accordingly), a reduction in the magnetic field strength by  $\gtrsim 67\%$ , and an increase in  $\dot{M}/v_w$  by a factor of  $\gtrsim 12$ .

## 6. Conclusions and Summary

Here we report the early optical discovery of SN 2020oi and present a detailed panchromatic set of measurements of the SN. In the optical we find that SN 2020oi is a normal young SN Ic with early photospheric velocity of  $\sim 15,000 \text{ km s}^{-1}$ . The series

<sup>31</sup> The peak of the bolometric luminosity is at an earlier time than the time when we estimate  $\epsilon_B$  above, hence the difference in luminosity values.

of optical spectra that we present shows a typical evolution of a stripped envelope SN. In X-rays, observations undertaken by the Swift satellite did not reveal any bright X-ray SN emission. However, the sensitivity of the X-ray observations is limited by the bright existing background emission from the host galaxy. Thus the X-ray observations only provide a weak constraint of  $L_X \lesssim 10^{40}$  erg s $^{-1}$ . In the radio a bright mJy source is detected in observations undertaken by several facilities.

The radio observations we present in this paper were undertaken by the VLA, ATCA, e-MERLIN, and the AMI-LA telescopes. The observations resulted in multi-epoch multi-frequency detailed measurements. We analyze these measurements in several ways assuming a model of a single shock wave driven by the interaction of the SN ejecta with the CSM (Chevalier 1998). We performed modeling of the radio data in several ways, including single-epoch spectral modeling, single-frequency modeling, and spectral multi-epoch modeling.

Our modeling of the radio data points toward a non-equipartition shock wave traveling in a dense CSM environment. We find that on average the shock wave is moving at a constant velocity, although a standard constant-velocity shock-wave model alone fails to reproduce the full data set. This may be explained by a slight deviation of the CSM density structure from an  $r^{-2}$  power-law function. If this is indeed the case, it may suggest that the mass-loss rate had been slowly changing. However, the lack of detailed high-resolution data at low gigahertz frequencies limits the analysis performed here and does not allow a more complex modeling.

Our radio data set also exhibits a period in which the spectral index in the optically thin regime becomes rather steep. A possible explanation is the effect of electron cooling by the inverse Compton process on the observed spectrum. After about 40 days, the spectral index becomes shallower and reaches a value of  $\beta \approx -1$ , which is the typical spectral index observed in stripped envelope SNe when cooling is not in play. We use the departure of the inverse Compton cooling from our observing bands at  $\sim 40$  days to estimate the ratio between two key microphysical parameters,  $\epsilon_e/\epsilon_B \gtrsim 200$ . Also, the relation between the spectral index  $\beta$  and the power-law index  $p$  of the electron energy distribution,  $\beta = -(p - 1)/2$ , is valid in the absence of electron cooling, i.e., after  $\sim 40$  days. This points to an index of  $p \approx 3$ , which is the typical index observed in SNe Ic (Chevalier & Fransson 2006).

Large deviations from equipartition in SN-CSM shock waves have been observed in the past in several cases (e.g. SN 2011dh, Soderberg et al. 2012; Horesh et al. 2013b; SN 2012aw, Yadav et al. 2014; SN 2013df, Kamble et al. 2016), although in other cases the shock wave was found to be in equipartition (e.g., Bjornsson & Fransson 2004). Early high-cadence panchromatic observations played a key role in identifying these deviations. In many other cases, there is not enough information to determine whether there is a deviation from equipartition. In these cases, the derived shock-wave and CSM parameters may not truly represent their real values. Here, for example, the estimate of shock-wave velocity is lowered from  $\approx 4 \times 10^4$  km s $^{-1}$  to  $\approx 3 \times 10^4$  km s $^{-1}$  when taking into account the deviation from equipartition. As for the estimate of mass-loss rate, the effect on it is much greater, and in our case it increases by a factor of  $> 12$ . The question of why some SN shock waves exhibit equipartition while others show large deviations from equipartition still remains open. Before

attempting to answer this question, a better characterization of a large sample of SNe at early times is needed.

Overall, SN 2020oi is a normal SN Ic in optical wave bands, with a somewhat nonstandard evolution of its radio emission. The SN-CSM shock wave we find in our analysis suggests velocities in the range of  $(3\text{--}4) \times 10^4$  km s $^{-1}$ , which is typical of SNe Ic. The mass-loss rate we deduce including the deviation from equipartition is at the higher end of the mass-loss rate in stripped envelope SNe, but not in any extreme way (Smith 2014). Detailed panchromatic observational campaigns, such as the one undertaken here, are required to build a large sample of well-characterized stripped envelope SNe that may be used to search for answers to some of the open questions in the field of SNe.

We thank the anonymous referee. A.H. is grateful for the support by grants from the Israel Science Foundation, the US–Israel Binational Science Foundation (BSF), and the I-CORE Program of the Planning and Budgeting Committee and the Israel Science Foundation. T.M. acknowledges the support of the Australian Research Council through grant FT150100099. D.D. is supported by an Australian Government Research Training Program Scholarship. D.R.A.W. was supported by the Oxford Centre for Astrophysical Surveys, which is funded through generous support from the Hintze Family Charitable Foundation. A.A.M. is funded by the Large Synoptic Survey Telescope Corporation, the Brinson Foundation, and the Moore Foundation in support of the LSSTC Data Science Fellowship Program; he also receives support as a CIERA Fellow by the CIERA Postdoctoral Fellowship Program (Center for Interdisciplinary Exploration and Research in Astrophysics, Northwestern University). M.P.T. acknowledges financial support from the State Agency for Research of the Spanish MCIU through the “Center of Excellence Severo Ochoa” award to the Instituto de Astrofísica de Andalucía (SEV-2017-0709) and through grant PGC2018-098915-B-C21 (MCI/AEI/FEDER, UE). J.M. acknowledges financial support from the State Agency for Research of the Spanish MCIU through the “Center of Excellence Severo Ochoa” award to the Instituto de Astrofísica de Andalucía (SEV-2017-0709) and from the grant RTI2018-096228-B-C31 (MCIU/FEDER, EU). A.G.Y.’s research is supported by the EU via ERC grant No. 725161, the ISF GW excellence center, an IMOS space infrastructure grant and BSF/Transformative and GIF grants, as well as The Benoziyo Endowment Fund for the Advancement of Science, the Deloro Institute for Advanced Research in Space and Optics, The Veronika A. Rabl Physics Discretionary Fund, Paul and Tina Gardner, Yeda-Sela and the WIS-CIT joint research grant; A.G.Y. is the recipient of the Helen and Martin Kimmel Award for Innovative Investigation. M.R. has received funding from the European Research Council (ERC) under the European Union’s Horizon 2020 research and innovation program (grant agreement n759194—USNAC). M.W.C. acknowledges support from the National Science Foundation with grant number PHY-2010970. C.F. gratefully acknowledges support of his research by the Heising-Simons Foundation (#2018-0907). Based on observations obtained with the Samuel Oschin Telescope 48 inch and the 60 inch Telescope at the Palomar Observatory as part of the Zwicky Transient Facility project. Z.T.F. is supported by the National Science Foundation under grant No. AST-1440341 and a collaboration including Caltech, IPAC, the Weizmann Institute

for Science, the Oskar Klein Center at Stockholm University, the University of Maryland, the University of Washington, Deutsches Elektronen-Synchrotron and Humboldt University, Los Alamos National Laboratories, the TANGO Consortium of Taiwan, the University of Wisconsin at Milwaukee, and Lawrence Berkeley National Laboratories. Operations are conducted by COO, IPAC, and UW. Partly based on observations made with the Nordic Optical Telescope. SED Machine is based upon work supported by the National Science Foundation under grant No. 1106171. The National Radio Astronomy Observatory is a facility of the National Science Foundation operated under cooperative agreement by Associated Universities, Inc. The Australia Telescope Compact Array is part of the Australia Telescope National Facility which is funded by the Australian Government for operation as a National Facility managed by CSIRO. We acknowledge the Gomeroi people as the traditional owners of the Observatory site. e-MERLIN is a National Facility operated by the University of Manchester at Jodrell Bank Observatory on behalf of STFC. We thank the staff of the Mullard Radio Astronomy Observatory for their assistance in the commissioning, maintenance, and operation of AMI, which is supported by the Universities of Cambridge and Oxford. We also acknowledge support from the European Research Council under grant ERC-2012-StG-307215 LODESTONE. This work was supported by the GROWTH project funded by the National Science Foundation under grant No. 1545949.

**Software:** ZTF pipeline (Masci et al. 2019), LCO pipeline (Fremling et al. 2020), pySEDM (Rigault et al. 2019), NOT and P200 pipelines (Bellm & Sesar 2016), CASA (McMullin et al. 2007), AMI-LA data reduction package (Perrott et al. 2013), MIRIAD standard routines (Sault et al. 1995), wsclean (Offringa et al. 2014), HEAsoft (Blackburn 1995).

## Appendix A Analysis of AMI-LA Data

In Section 3.5 we discussed the low angular resolution of AMI-LA and the resulting quiescent underlying emission from the area surrounding the SN. To estimate this excess emission, we assume that the optically thin regime of the AMI-LA light curve behaves as a power law in time plus a constant. To estimate the power-law index we fit the data acquired 11–22 days after explosion, in the K, Ka, and Q bands, to a power-law function of time. We use only this time period since the flux measured by AMI-LA at later times is plateauing and probably represents the somewhat constant quiescent emission. In addition, as we show in Section 5.4, electron cooling is important in this time range, while later it becomes negligible. We then average all these power laws to get an average power-law index of  $b_{\text{avg}} = -1.66 \pm 0.28$ .

We now fit the emission measured by AMI-LA in the optically thin regime 11.76–21.56 days after explosion with the simple function  $F_{\nu} = At^{b_{\text{avg}}} + C$ . The result of this fit is  $C = 8.0 \pm 1.1$  mJy ( $\chi^2_r = 0.23$ , dof = 6), and it is shown in Figure 9. Hence, we estimate the underlying constant emission evident in AMI-LA observations to be  $8.0 \pm 1.1$  mJy. Note that the temporal power-law is expected to evolve over time (as evident in Section 5.2 from fitting the temporal power laws in two different time periods) and the AMI fitting process does not

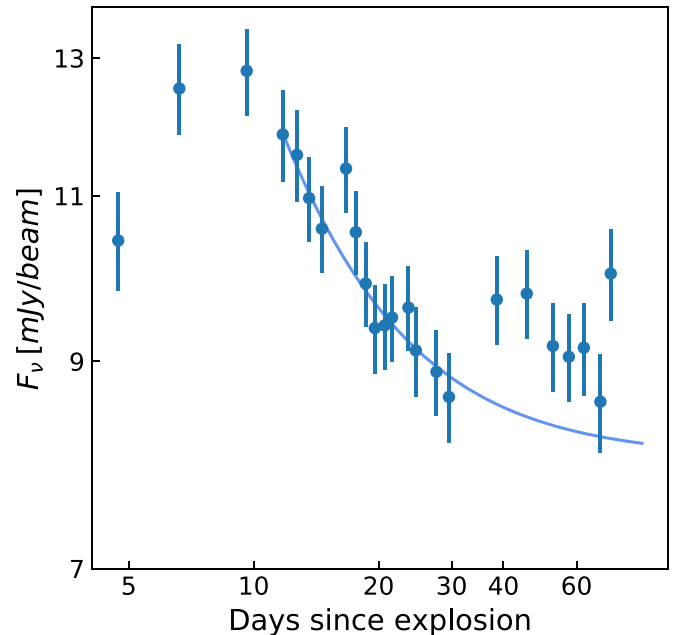


**Figure 9.** Radio emission as measured by AMI-LA and reported in Table 2. Also plotted are the results of the fitting process we conducted to estimate the constant underlying emission as described in Section 5.2. The power-law index of the flux with time,  $b_{\text{avg}} = -1.66 \pm 0.28$ , is an average of the power laws for the different K, Ka, and Q sub-bands. The coefficient  $A = 233 \pm 54$  and the constant  $C = 8.0 \pm 1.1$  mJy are products of the fit of the function  $F_{\nu} = At^{b_{\text{avg}}} + C$  to the flux measured by AMI-LA in the optically thin regime.

take this fully into account, because we lack information about this varying evolution in the AMI band. Moreover, the flux from the quiescent sources that contaminate the AMI measurement may experience slight variations that also affect the results here.

We subtract the constant emission based on the above estimate and fit Equation (4) in Chevalier (1998) to the 15.5 GHz light curve measured by AMI-LA, similar to the fit we performed to the e-MERLIN data (see Section 5.2). We use AMI-LA measurements from the first detection to 21.56 days after explosion only. The resulting power-law indices are  $a = 2.1 \pm 1.6$  and  $b = -1.75 \pm 0.52$ . The fitted peak flux at 15.5 GHz is  $F_{\nu_a} = 5.33 \pm 1.61$  mJy, 8.39 ± 1.49 days after explosion ( $\chi^2_r = 0.72$ , dof = 7). We used the peak at 15.5 GHz to calculate  $R$ ,  $B$ ,  $v_{\text{sh}}$ , and  $\dot{M}$  (assuming  $p = 3$ ,  $v_{\text{sh}} = R/t_a$ , and  $v_w = 1000$  km s<sup>-1</sup>) and find a rough (due to a large uncertainty) estimate of the shock-wave velocity of  $v_{\text{sh}} \approx (4.8 \pm 1.4) \times 10^4$  km s<sup>-1</sup>. While this velocity is somewhat higher than the velocities we derived earlier on, this result is consistent within  $1\sigma$  with the previously measured velocities (see Table 4). Moreover, as we note above, the fitting of the AMI data should be treated with caution and so should any estimated property that is based on it.

## Appendix B VLA Sub-band Measurements

VLA sub-band measurements are given in Table 5.

**Table 5**  
VLA Sub-band Observations of SN 2020oi

Time (days)	Frequency (GHz)	Flux (mJy beam <sup>-1</sup> )	e_Flux (mJy beam <sup>-1</sup> )	rms (mJy)
5.15	41	5.25	0.54	0.05
5.15	43	5.10	0.52	0.06
5.15	45	4.86	0.50	0.07
5.15	47	4.94	0.52	0.08
6.03	13	2.88	0.29	0.01
6.03	15	3.24	0.33	0.01

**Note.** A summary of the radio flux measurements of the VLA sub-band data. The columns from left to right are as follows: time since explosion in days; observed central frequency in GHz; peak flux density in mJy beam<sup>-1</sup>; uncertainty of the peak flux density in mJy beam<sup>-1</sup>; image rms in mJy.

(This table is available in its entirety in machine-readable form.)

## ORCID iDs

- Assaf Horesh <https://orcid.org/0000-0002-5936-1156>  
 Itai Sfaradi <https://orcid.org/0000-0003-0466-3779>  
 Cristina Barbarino <https://orcid.org/0000-0002-3821-6144>  
 Jesper Sollerman <https://orcid.org/0000-0003-1546-6615>  
 Javier Moldon <https://orcid.org/0000-0002-8079-7608>  
 Dougal Dobie <https://orcid.org/0000-0003-0699-7019>  
 Steve Schulze <https://orcid.org/0000-0001-6797-1889>  
 Miguel Pérez-Torres <https://orcid.org/0000-0001-5654-0266>  
 David R. A. Williams <https://orcid.org/0000-0001-7361-0246>  
 Christoffer Fremling <https://orcid.org/0000-0002-4223-103X>  
 Avishay Gal-Yam <https://orcid.org/0000-0002-3653-5598>  
 Shrinivas R. Kulkarni <https://orcid.org/0000-0001-5390-8563>  
 Andrew O'Brien <https://orcid.org/0000-0003-4609-2791>  
 Peter Lundqvist <https://orcid.org/0000-0002-3664-8082>  
 Tara Murphy <https://orcid.org/0000-0002-2686-438X>  
 Eric C. Bellm <https://orcid.org/0000-0001-8018-5348>  
 Michael W. Coughlin <https://orcid.org/0000-0002-8262-2924>  
 V. Zach Golkhou <https://orcid.org/0000-0001-8205-2506>  
 Matthew J. Graham <https://orcid.org/0000-0002-3168-0139>  
 Dave A. Green <https://orcid.org/0000-0003-3189-9998>  
 Thomas Kupfer <https://orcid.org/0000-0002-6540-1484>  
 Russ R. Laher <https://orcid.org/0000-0003-2451-5482>  
 Frank J. Masci <https://orcid.org/0000-0002-8532-9395>  
 A. A. Miller <https://orcid.org/0000-0001-9515-478X>  
 James D. Neill <https://orcid.org/0000-0002-0466-1119>  
 Eran O. Ofek <https://orcid.org/0000-0002-6786-8774>  
 Yvette Perrott <https://orcid.org/0000-0002-6255-8240>  
 Mickael Rigault <https://orcid.org/0000-0002-8121-2560>  
 Ben Rusholme <https://orcid.org/0000-0001-7648-4142>  
 David L. Shupe <https://orcid.org/0000-0003-4401-0430>  
 David Titterington <https://orcid.org/0000-0003-1431-920X>

## References

- Ahn, C. P., Alexandroff, R., Allende Prieto, C., et al. 2014, *ApJS*, 211, 17  
 Becker, R. H., White, R. L., & Helfand, D. J. 1994, *adass III*, 61, 165  
 Bellm, E. C., Kulkarni, S. R., Barlow, T., et al. 2019, *PASP*, 131, 068003  
 Bellm, E. C., & Sesar, B. 2016, pyraf-dbsp: Reduction pipeline for the Palomar Double Beam Spectrograph, Astrophysics Source Code Library, ascl:1602.002